Journal of Sol-Gel Science and Technology (2022) 102:18–29
https://doi.org/10.1007/s10971-021-05638-3

INVITED PAPER: SOL-GEL AND HYBRID MATERIALS WITH SURFACE MODIFICATION FOR APPLICATIONS

Mesoporous structured silica modified with niobium oxide and cobalt hematoporphyrin applied to the simultaneous electrochemical evaluation of oxalic and uric acids

Luana V. Souza[1] · Anike H. Virgili[1] · Guilherme O. Teixeira[1] · Ruth Hinrichs[2] · Daniela Bianchini[3] · Tania M. H. Costa[1] · Leliz T. Arenas[1] · Edilson V. Benvenutti[1] · Eliana W. de Menezes[1]

Received: 29 April 2021 / Accepted: 1 September 2021 / Published online: 28 October 2021

Abstract

Mesoporous SBA-15-type silica, with cylindrical pores hexagonally ordered, was obtained and modified with niobium oxide in a highly dispersed way. Subsequently, a further modification with cobalt hematoporphyrin was performed. The ordered pore structure of the SBA-15 was preserved after successive modifications, maintaining its textural properties. The material was used to modify a carbon paste electrode that was successfully applied to the individual and simultaneous detection of both oxalic acid and uric acid, by using cyclic voltammetry and differential pulse voltammetry. For individual evaluation, the obtained detection limits for oxalic acid and uric acid were 9.94 and 0.17 μmol·L^{-1}, respectively. However, for the simultaneous evaluation of both analytes, the detection limits were 2.83 and 0.14 μmol·L^{-1}, for oxalic acid and uric acid, respectively.

Graphical Abstract

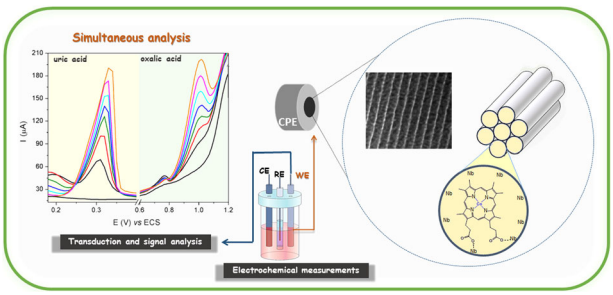

Keywords Santa Barbara Amorphous materials · Niobia · Sol-gel · Grafting · Electrochemical sensor · CPE

Highlights

- Well-ordered silica grafted with niobia and cobalt hematoporphyrin.
- SBA-15 texture preserved after successive modifications with niobium oxide and hematoporphyrin macromolecule.
- Simultaneous electrochemical evaluation of oxalic acid and uric acid.
- Modified carbon paste electrode for sensitive evaluation of uric and oxalic acids.

✉ Edilson V. Benvenutti
benvenutti@ufrgs.br

✉ Eliana W. de Menezes
eliana.weber@ufrgs.br

[1] LSS - Laboratory of Solids and Surfaces, Instituto de Química, UFRGS, CP 15003, CEP 91501-970, Porto Alegre, RS, Brazil

[2] Instituto de Geociências, UFRGS, Porto Alegre, RS, Brazil

[3] Centro de Ciências Químicas, Farmacêuticas e de Alimentos, UFPel, Pelotas, RS, Brazil

1 Introduction

Mesoporous SBA-15-type silica materials exhibit high surface area and cylindrical hexagonally ordered mesopores [1]. The preparation of this type of material is based on the hydrolysis and polycondensation reactions of silicon alkoxide precursors and a template is employed to build the well-organized pore structure. This synthesis strategy allows specific textural characteristics to be obtained that lead to materials with high pore volumes, unimodal pore size distributions and interconnected micropores and mesopores [2] which allow their use as sorbents [3], catalysts [4, 5], drug delivery systems [6], as well as matrices for the development of electrochemical sensors [7]. Such silica moieties with high surface areas and high pore volumes led to a high electroactive area, which is an important parameter to obtain efficient electrodes. It was demonstrated that the best silica materials for manufacturing CPEs were ordered systems, such as SBA-15, which presents high porosity, interconnected micropores and cylindrical mesopores, enabling electron transfer and allowing the easy diffusion of species to specific sites [8].

SBA-15 silica materials can be chemically modified by grafting reactions to produce metal oxide coatings covalently bonded to the silica surface [9]. By using planned and well-controlled experimental conditions, the grafting reactions allow highly dispersed and amorphous metal oxides to be obtained, in this way preventing pore blocking and maintaining the textural characteristics of the SBA-15 silica matrix [10, 11]. In the same way, the modification of silica surfaces with thin coatings of metal oxides, such as niobium oxide, provides reactive Lewis and Brønsted acid sites [11–13]. These sites facilitate enabling interactions with other species with specific organic functional groups, such as carboxylate [14] and allow the immobilization of electroactive macromolecules [9, 15], which is useful for the development of electrochemical sensors.

Despite exhibiting high solubility, oxalic acid chelation with calcium or magnesium leads to the formation of oxalate salts, which have rather low solubility. This process, in addition to removing calcium ions from the blood, can produce renal stones [16, 17]. In this way, the urinary level of oxalic acid has been recognized as an indicator in the diagnosis of renal stones. Another important compound that is present in the human organism is uric acid, which is the product of purine metabolism. The amount of uric acid in the blood or urine also helps to diagnose several diseases, such as hyperuricemia, Lesch–Nyhan syndrome, obesity, gout, diabetes, high blood pressure, and high cholesterol [18, 19]. Several methods have been described to quantify oxalic and uric acids in body fluids, including spectrometry [20, 21] and chemiluminescence [22, 23]. However, these methods are expensive and they involve several sampling steps. Thus, simple and direct methods for monitoring the amount of oxalic and uric acids are desirable. Therefore, electrochemical techniques stand out as being easy and low-cost possibilities. In this context, this work presents a CPE modified with mesoporous SBA-15 material, previously grafted with niobium oxide and cobalt hematoporphyrin (CoHp), which allows the evaluation of these analytes individually or simultaneously. As far as we know, this is the first report of simultaneous evaluation of oxalic acid and uric acid, making the developed electrode very promising for application in diagnosis for both analytes that are simultaneously present in urine.

2 Experimental

2.1 Synthesis of SBA-15

SBA-15 type silica was synthesized from an adapted procedure reported elsewhere [1]. In this procedure, Pluronic® P-123 surfactant was used as a template and tetraethylorthosilicate (TEOS, Sigma, 98%) as a source of silica. For the purpose of this synthesis, 2 g of surfactant were first dissolved in 75 mL of 1.6 mol·L^{-1} HCl (Merck). The system was maintained at 40 °C under magnetic stirring. Afterward, 4.6 mL of TEOS were added slowly and the system remained under stirring and heating for 24 h. Then the system was transferred to an autoclave and heated at 100 °C for an additional 24 h. The white solid obtained was filtered, washed with distilled water, and dried in an oven at 80 °C for 4 h. Finally, the material was calcined in a muffle furnace for 6 h at 550 °C to remove the template. This procedure was repeated several times to obtain a sufficient amount of SBA-15 material.

2.2 Modification of SBA-15 surface with niobium oxide (SBA/Nb)

SBA-15 material (2.5 g) was previously activated at 120 °C, under vacuum, for 8 h. Subsequently, it was dispersed in toluene (Merck, 99.5%, 30 mL), under N_2 atmosphere, at 80 °C. At the same time, 405 mg of niobium pentachloride, provided by Companhia Brasileira de Mineração e Metalurgia (CBMM) were dissolved in 10 mL of absolute ethanol (Merck, 99.9%), in a glove chamber, under N_2 atmosphere. This solution was added to the flask containing SBA-15 in toluene. The mixture remained under mechanical stirring at 80 °C for 18 h. Afterwards, the supernatant was removed, and the material was washed with the following order of solvents: toluene, ethanol, water, and ethanol. The solid was then

dried at 120 °C, under vacuum. This material is hereafter called SBA/Nb.

2.3 Modification of SBA/Nb with cobalt hematoporphyrin (SBA/Nb/HpCo)

Firstly, the metalation of hematoporphyrin was performed by adapting the method described by Zahavi [24]. Hematoporphyrin (50 mg) was dissolved in 5 mL of chloroform and 7 mL of tetrahydrofuran (Merck). A cobalt acetate (Synth, 50 mg)/acetic acid solution (Dynamics, 4 mL) was added, under N_2 atmosphere and the system maintained under stirring, for 4 h. A mixture of acetic acid:ethyl acetate (1:8 v/v) was then added to precipitate the excess of cobalt, which was separated by centrifugation. Hexane (Merck, 16 mL) was added to the supernatant and the system was left in the refrigerator at 5 °C for 24 h. A CoHp precipitate thus formed was separated by centrifugation, dried under vacuum, and redissolved in 10 mL of ethanol. The CoHp ethanolic solution was added to 2.0 g of SBA/Nb material. The system was maintained under mechanical stirring for 24 h. Finally, the solid was filtered, washed with ethanol and dried at 100 °C under vacuum. The solid obtained was designated as SBA/Nb/HpCo.

2.4 Materials characterization

X-ray diffraction analysis (XRD) was performed using a Siemens model D500 diffractometer, with Cu-Kα as source ($\lambda = 0.154056$ nm). The N_2 isotherms were obtained at 77 K, using a Tristar II Kr Micromeritics instrument, after the samples were degassing at 120 °C, for 10 h. BET surface area and BJH pore size distribution methods were applied [25]. Transmission electron microscopy (TEM) images were obtained using a JEOL JEM model 2010, operating at 120 keV. The samples were previously dispersed in isopropyl alcohol, in an ultrasound bath, and dispersed onto a carbon-coated copper grid, before the analyses. Scanning electron microscopy (SEM) images were acquired in a Zeiss Auriga microscope. The samples were previously dispersed on a conductive tape on aluminum support and coated with gold film. EDS analysis was acquired with an electron beam of 15 keV and 5 nA current in a JEOL SEM with a LaB_6 filament and equipped with a Thermo Fisher Scientific SDD spectrometer. The samples were compacted as disks (5.0 ton cm^{-2}). UV-Vis spectra were obtained in an Agilent CARY 5000 spectrophotometer, using transmission technique for liquid samples and diffuse reflectance with integrating sphere for solid materials. The Kubelka-Munk method was applied in the latter case: $k/s = [(1-R)^2]/2R$, considering (R) as the diffuse reflectance, absorbed light as (k) and (s) as scattering coefficient.

2.5 Electrochemical measurements

Electrochemical measurements were performed on an IviumStat galvanostat/potentiostat by using a three-electrode cell constituted by: a saturated calomel electrode (SCE) as reference; a platinum wire as counter electrode and a CPE as a working electrode. The modified CPE was prepared by using SBA/Nb/HpCo material (8 mg), analytical grade graphite powder (Sigma, 99%, 12 mg) and mineral oil (5 mg). The components were mixed and a fraction of the paste was deposited in a Teflon cavity with 1 mm depth, connected to a platinum disk (6 mm of diameter) glued to a glass tube with a copper wire. The modified CPE is hereafter referred to as SBA/Nb/HpCo–CPE and was used to evaluate oxalic and uric acid contents (Sigma, 98%) using cyclic voltammetry and differential pulse voltammetry techniques. All measurements were carried out at room temperature in the presence of 1 mol L^{-1} KCl (Merck, 99.5%) as a support electrolyte. The potential range used for cyclic voltammograms for oxalic acid was between 0.3 and 1.0 V, with 20 mV·s^{-1} scan rate; for uric acid, the corresponding parameters were 0.1–0.6 V, and 20 mV·s^{-1}, respectively. For differential pulse voltammetry, the potential range used was between 0.1 and 0.4 V, with 5 mV·s^{-1} scan rate. Phosphate buffer solution (PBS, 0.1 mol·L^{-1}, pH 6.0) was prepared from NaH_2PO_4 (Vetec) and Na_2HPO_4 (Vetec).

3 Results and discussion

Niobium (V) oxide was grafted onto a mesoporous SBA-15 surface to generate the SBA/Nb material by using an anhydrous ethanolic $NbCl_5$ solution as niobium precursor. The grafting reaction was planned to yield 0.5 mmol of niobium per gram of SBA/Nb. Subsequently, this material was further modified with CoHp to obtain the SBA/Nb/HpCo. Figure 1A shows the XRD patterns of materials at small angles, from 0.5 to 2.8°. All diffractograms presented a typical pattern of mesoporous SBA–15 material with hexagonally ordered cylindrical pores. The peaks at 0.9°, 1.5°, and 1.7° angles are due to the 100, 110 and 200 planes, respectively [1, 5, 10]. The ordered cylindrical pore structure is illustrated in the inset Fig. 1A. The XRD results demonstrate that the hexagonal ordered structure of SBA-15 is preserved, even after the subsequent surface modifications with niobium oxide and CoHp. Figure 1B presents a SEM image of the SBA-15, showing silica particles with similar morphology with dimensions around 500 nm. The TEM image of SBA-15, which is depicted in Fig. 1C, shows a lateral view of the ordered structure of the cylindrical pores.

Figure 2A shows the backscattered electron image of the SBA/Nb/HpCo material and the EDS spectrum is depicted

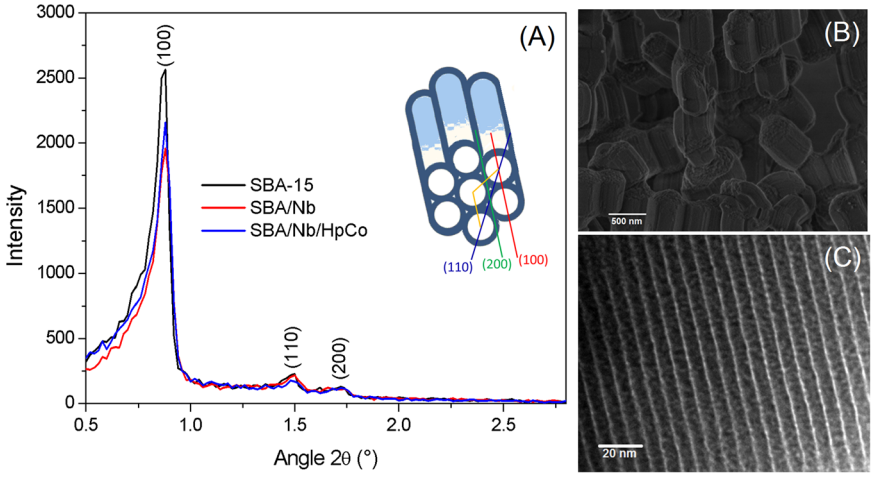

Fig. 1 **A** XRD analysis of SBA-15, SBA/Nb and SBA/Nb/HpCo materials. The Inset to (**A**) illustrates their cylindrical pore structure; **B** SEM image of SBA-15; **C** TEM image of SBA-15

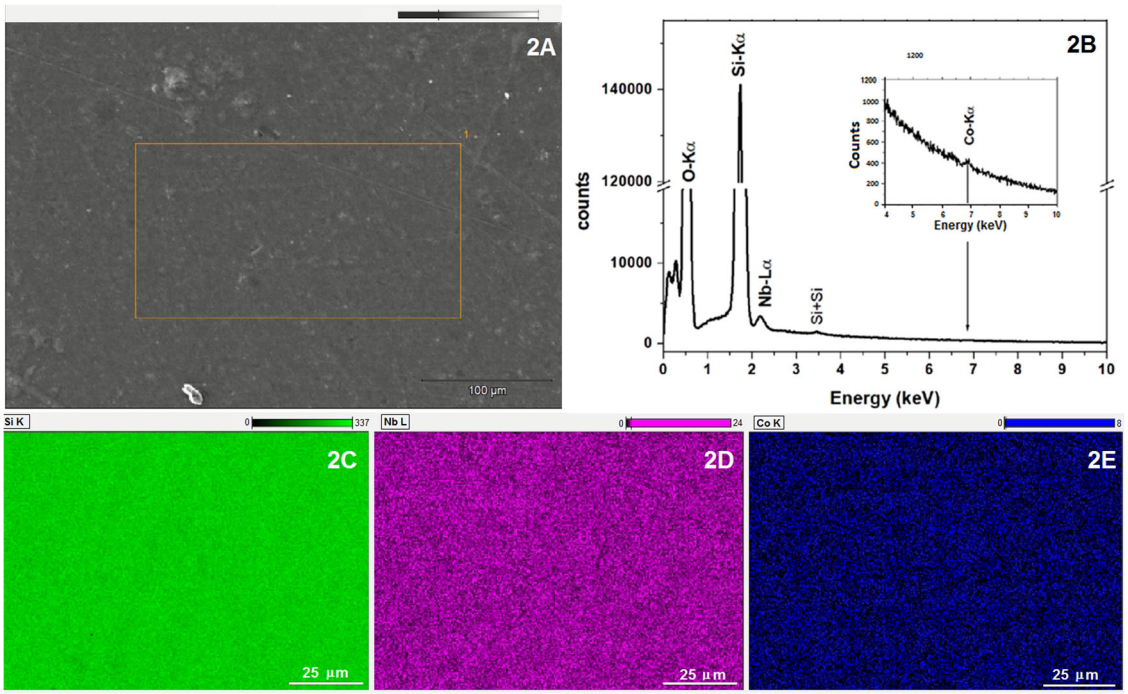

Fig. 2 EDS analysis: (**A**) backscattered electron image of sample pressed at 5.0 ton cm^2; **B** EDS spectrum; **C** silicon elemental mapping; **D** niobium elemental mapping and (**E**) cobalt elemental mapping

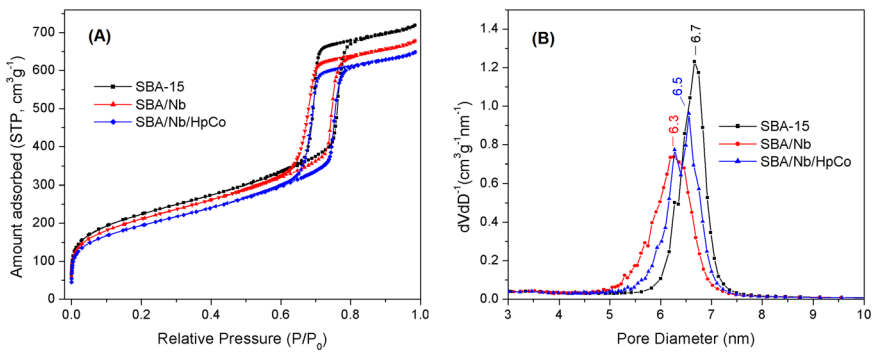

Fig. 3 Textural analysis of materials: (**A**) N_2 adsorption-desorption isotherms; **B** BJH pore size distribution, obtained from the desorption branch of isotherms

in Fig. 2B. The image is consistent with the pressed powder preparation of the sample (5.0 ton cm^2). The Si-Kα and Nb-Lα peaks are clearly observed, and they were estimated as 98 wt.% SiO_2 and 2 wt.% Nb_2O_5. In the case of the Co-Kα peak, quantification was not possible. Qualitatively, however, the presence of cobalt can be securely established. The elemental mapping is presented in Fig. 2C, 2D and 2E for silicon, niobium and cobalt, respectively. As can be seen, the niobium and the cobalt showed homogeneous distribution at the micrometric level, even though the latter is statistically poor.

Nitrogen adsorption-desorption isotherms are depicted in Fig. 3A. Type IV isotherms with vertical parallel H1 hysteresis are clearly seen for all materials. This behavior is typical of materials with cylindrical and highly ordered mesopores [1, 10]. The BJH pore size distribution curves shown in Fig. 3B, which were obtained from the desorption branch of isotherms, confirm the ordered mesopore structure with narrow size distribution, characteristic of SBA-15-type materials. The surface areas and pore diameters are presented in Table 1. After the grafting reaction, from SBA-15 to SBA/Nb, the surface area decreases by 5%, and the pore diameter decreases by 0.4 nm. This result indicates that the niobium oxide is highly dispersed on the surface (SBA/Nb), which is compatible with a coating of about 0.2 nm thickness [11]. Further modification of the surface with CoHp (SBA/Nb/HpCo) leads to an additional decrease in the surface area of about 8%, and also an increase of 0.2 nm in the pore diameter. This behavior, of increasing diameter, was already reported during the immobilization of macromolecules on porous silica materials, and it was interpreted as a possible leaching process which occurs during the CoHp immobilization, resulting in some erosion of the silica pore wall [26]. This interpretation makes sense, since the matrix for immobilizing CoHp (SBA/Nb) has not undergone previous heat treatment, precisely to remain

Table 1 Textural data of materials

Sample	Surface area (±5 m^2g^{-1})	Pore size[a] (nm)
SBA-15	768	6.7
SBA/Nb	730	6.3
SBA/Nb/HpCo	670	6.5

[a]Pore diameter, obtained from the maxima of the BJH pore distribution curves

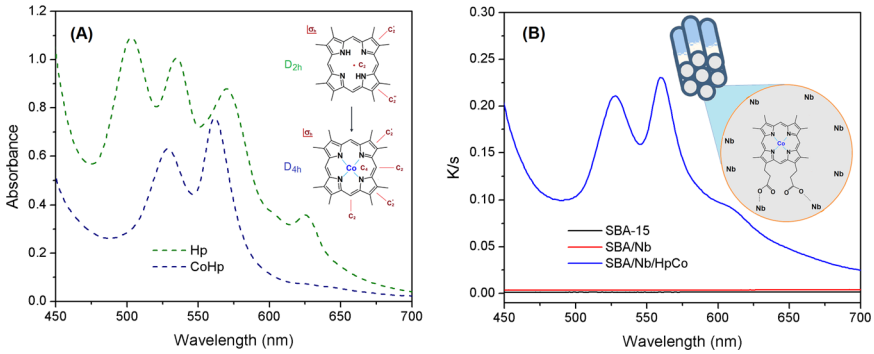

Fig. 4 UV-Vis spectra of: (**A**) ethanolic solution of hematoporphyrin (Hp) and cobalt hematoporphyrin (CoHp), the Inset shows their structures and symmetries; **B** solid materials, the inset shows a representation of cobalt hematoporphyrin functionalizing the SBA/Nb/HpCo pores

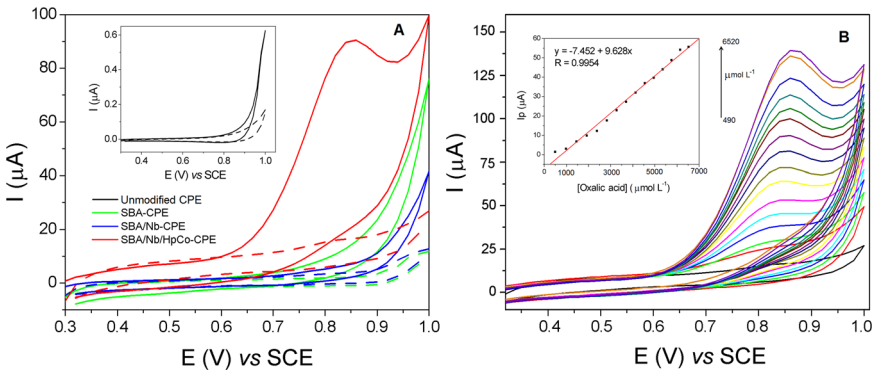

Fig. 5 **A** Cyclic voltammograms in the absence (segmented line) and in the presence of 4120 μmol L^{-1} of oxalic acid (straight line) for unmodified CPE, SBA-CPE, SBA/Nb-CPE and SBA/Nb/HpCo–CPE. **B** Cyclic voltammograms of SBA/Nb/HpCo–CPE in the presence of different concentrations (490 and 6520 μmol·L^{-1}) of oxalic acid, using 1 mol·L^{-1} of KCl and scan rate of 20 mV·s^{-1}; The Inset to (**B**) shows the linear correlation between peak current and oxalic acid concentration

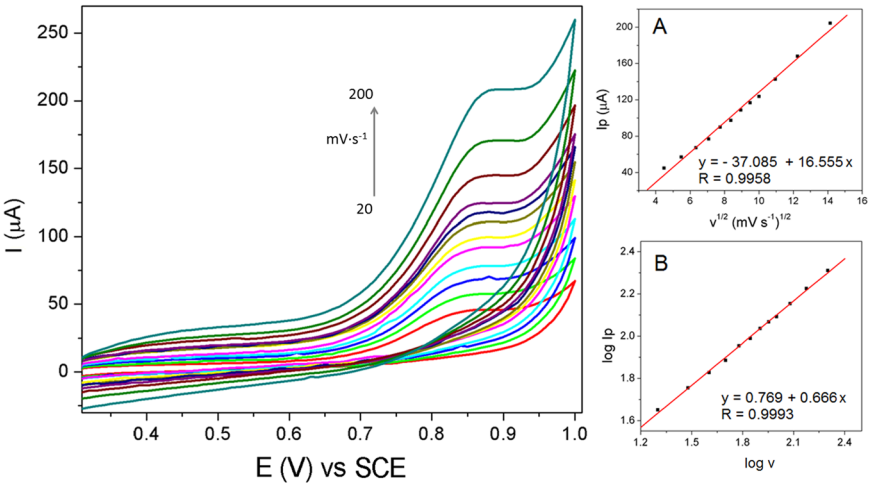

Fig. 6 Cyclic voltammograms obtained with SBA/Nb/HpCo–CPE at different scan rates (20–200 $mV \cdot s^{-1}$) in the presence of oxalic acid (4500 $\mu mol \cdot L^{-1}$), performed in 1 $mol \cdot L^{-1}$ KCl; **A** linear correlation between the current peak intensity (Ip) versus square root of the scan rate ($v^{1/2}$); **B** linear correlation between log Ip versus log v

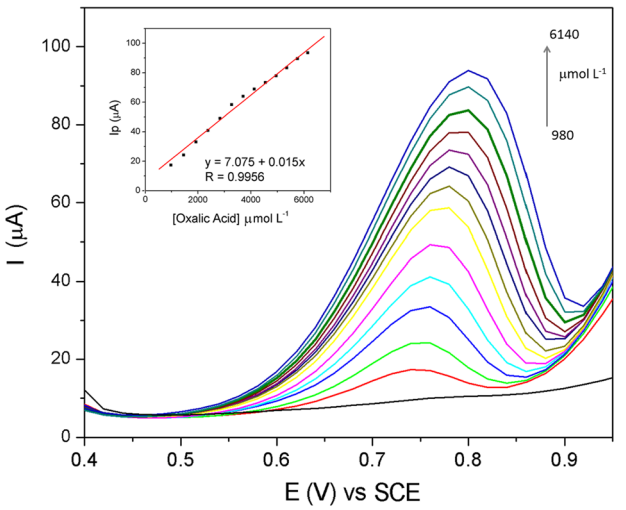

Fig. 7 Differential pulse voltammograms obtained with SBA/Nb/HpCo–CPE, in the presence of oxalic acid, in the concentration range from 980 to 6140 $\mu mol \cdot L^{-1}$, using 1 $mol \cdot L^{-1}$ KCl as support electrolyte and $v = 20\ mV \cdot s^{-1}$. The Inset shows the linear correlation between peak current and oxalic acid concentration

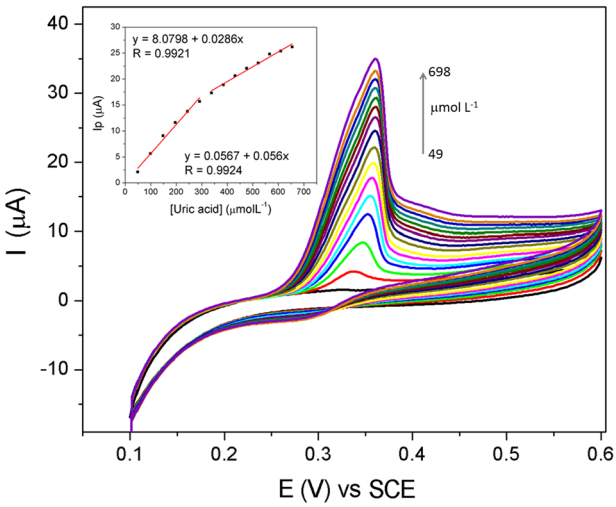

Fig. 8 Cyclic voltammograms obtained with SBA/Nb/HpCo–CPE in the presence of different concentrations of uric acid, in phosphate buffer solution (0.1 $mol \cdot L^{-1}$, pH 6), using 1 $mol \cdot L^{-1}$ KCl and $v = 20\ mV \cdot s^{-1}$. The inset shows the linear correlation between uric acid concentration and the intensity of the peak current

more reactive. In this way, the textural analysis is in accordance with the XRD data, showing that the successive surface modifications do not produce changes in the ordered pore structure and the texture of materials remains almost unchanged.

The UV-Vis spectra of hematoporphyrin before and after the metalation with cobalt are presented in Fig. 4A. The spectrum of hematoporphyrin presents four bands, assigned as Q bands of the porphyrin ring, associated with the D_{2h} symmetry, while the spectrum of metalated hematoporphyrin shows only two Q bands, which are associated with the D_{4h} symmetry [27–29]. The spectrum of SBA/Nb/HpCo material is depicted in Fig. 4B. Two Q bands are evident in the latter spectrum, identifying the presence of the CoHp in which the porphyrin ring presents D_{4h} symmetry. The spectra of SBA-15 and SBA/Nb materials show no bands in the visible region (Fig. 4B).

The SBA/Nb/HpCo material was used to modify the CPE (SBA/Nb/HpCo–CPE) in order to verify the viability of its use in the electrochemical determination of oxalic and uric acids. Firstly, cyclic voltammograms were obtained in the absence and in the presence of oxalic acid for unmodified CPE, SBA-CPE, SBA/Nb-CPE and SBA/Nb/HpCo–CPE, using 1 $mol \cdot L^{-1}$ KCl solution as electrolyte support. The resulting cyclic voltammograms are shown in Fig. 5A. For all the electrodes, no oxidation peak was detected in the absence of oxalic acid, in the potential range studied. However, for SBA/Nb/HpCo–CPE, in the presence of oxalic acid, a well-defined irreversible anodic peak, which corresponds to its oxidation, was observed at a

Table 2 Comparative performance of different electrodes in the electrochemical determination of oxalic acid

Electrode	Experimental conditions	Electrochemical techniques	Linear range ($\mu mol \cdot L^{-1}$)	LOD ($\mu mol \cdot L^{-1}$)	Reference
Graphite/Ag/AgCl[a]	H_3PO_4 (0.05 M) $v = 350\ mV \cdot s^{-1}$	EIS, CV, DPV	10–750	3.7	[31]
TiO_2/MWCNTs/GC[b]	$HClO_4$ (0.1 M) $v = 50\ mV \cdot s^{-1}$	CV	100–10000	33	[35]
PdAuNP/graphene[c]	H_2SO_4 (0.2 M) $v = 100\ mV \cdot s^{-1}$	CV, LSV	5–100	2.7	[36]
Pd/SBA-15/CPE[d]	H_2SO_4 (0.1 M)/0.1 M PBS (pH 6.00) $v = 50\ mV \cdot s^{-1}$	CV, LSV	10–140	0.4	[37]
PtNP/Glassy Carbon[e]	$HClO_4$ (0.1 M) $v = 100\ mV \cdot s^{-1}$	CV, Amperometry	1.4–595	0.28	[38]
Ag-doped ZSM-5[f]	PBS (0.1 M) $v = 20\ mV \cdot s^{-1}$	CV, DPV	16–1800	5.5	[39]
PdNP/rGO[g]	H_2SO_4 (0.1 M) $v = 50\ mV \cdot s^{-1}$	CV, DPV	50–10,000	50	[40]
AgNRs/Graphene[h]	PBS (0.1 M) $v = 50\ mV \cdot s^{-1}$	CV	3000–30,000	40	[41]
PdPt/GC[i]	$HClO_4$ (0.1 M) $v = 100\ mV \cdot s^{-1}$	CV, Amperometry	10–4700	1	[42]
SBA/Nb/HpCo–CPE	KCl (1 M) $v = 20\ mV \cdot s^{-1}$	CV, DPV	980–6140	9.94	This work
SBA/Nb/HpCo–CPE[j]	KCl (1 M) $v = 20\ mV \cdot s^{-1}$	CV, DPV	1456–4128	2.83	This work

LOD Limit of detection, *EIS* Electrochemical impedance spectroscopy, *CV* Cyclic voltammetry, *DPV* Differential pulse voltammetry, *LSV* Linear sweep voltammetry, v = scan rate

[a]Silver and silver chloride deposited on graphite

[b]TiO_2 nanoparticles/multi-walled carbon nanotubes/glassy carbon

[c]Palladium nanoparticles on reduced graphene oxide

[d]Palladium-doped SBA/carbon paste electrode

[e]Platinum nanoparticles modified glassy carbon electrode

[f]Silver incorporated in ZSM-5/carbon paste electrode

[g]Palladium nanoparticles on reduced graphene oxide

[h]Silver nanorods dispersed on graphene

[i]Palladium and Platinum/glassy carbon

[j]Simultaneous analysis with Uric Acid

potential near to 0.85 V. For all other electrodes no oxalic acid oxidation peak was observed, in the potential range studied. These results confirm the electrocatalytic properties of the SBA/Nb/HpCo–CPE system. The peak irreversibility is due to the formation of carbon dioxide during the oxidation, which is rapidly released from the electrode's surface, thus making the process irreversible [30, 31].

The cyclic voltammograms of SBA/Nb/HpCo–CPE, obtained by using different oxalic acid concentrations, in the range between 490 and 6520 $\mu mol \cdot L^{-1}$, are shown in Fig. 5B. An increase in the intensity of the acid oxalic oxidation peak was observed with increasing oxalic acid concentration and the inset Fig. 5B shows the linear correlation between the anodic peak current and the analyte concentration, considering only the Faradaic current. In this way, it is revealed that this electrode has potential applicability as a sensor, within the chosen concentration range.

With the purpose of evaluating the electrochemical behavior of the SBA/Nb/HpCo–CPE, in the oxalic acid oxidation, cyclic voltammograms were performed with different scan rates, between 20 and 200 $mV \cdot s^{-1}$, in the presence of 1.0 $mol \cdot L^{-1}$ KCl solution. The voltammograms are shown in Fig. 6. The linear correlation between the current peak intensity (Ip) and the square root of the scan rate (Fig. 6A) suggests a diffusional mechanism for the electroactive species on the electrode surface. The correlation between log v versus log Ip was obtained in order to confirm whether the process is really controlled by diffusion. A slope close to 0.5 indicates a

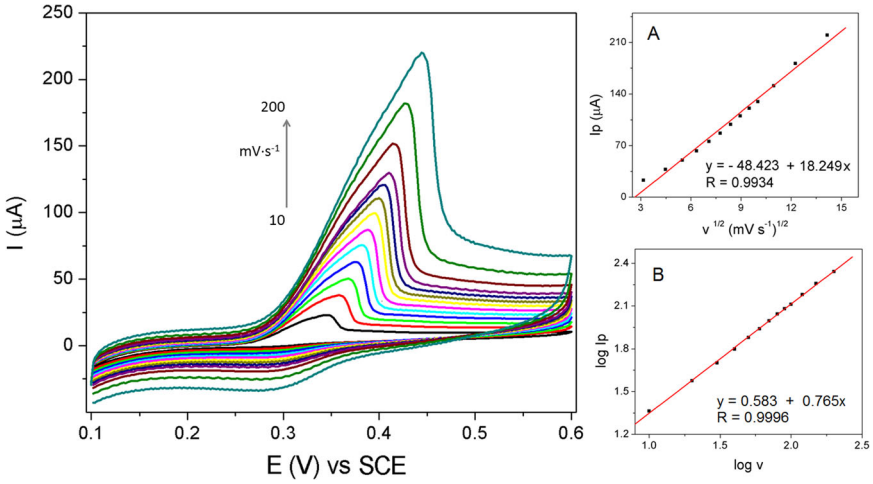

Fig. 9 Cyclic voltammograms obtained with SBA/Nb/HpCo–CPE at different scan rates (10–200 $mV \cdot s^{-1}$) in the presence of uric acid (698 $\mu mol \cdot L^{-1}$), using phosphate buffer (0.1 $mol \cdot L^{-1}$, pH 6) and 1 $mol \cdot L^{-1}$ KCl; **A** linear correlation between the current peak intensity (Ip) versus square root of the scan rate ($v^{1/2}$); **B** linear correlation between log Ip versus log v

diffusional process, while a slope value close to 1.0 indicates that the process occurs by adsorption [32, 33]. As the obtained linear correlation value was 0.666 (Fig. 6B), we can infer that the oxidation process of the oxalic acid on the SBA/Nb/HpCo–CPE is controlled by a diffusion mechanism, because the slope is near 0.5.

Measurements using differential pulse voltammetry techniques, with the SBA/Nb/HpCo-CPE electrode, were performed with concentrations of oxalic acid between 980 and 6140 $\mu mol \cdot L^{-1}$. The voltammograms are depicted in Fig. 7, and they show that the anodic peak current increases with increasing oxalic acid concentration. The inset to Fig. 7 shows the linear correlation between the anodic peak current and the oxalic acid concentration. According to the slope of this curve, the sensitivity was estimated as 0.015 $\mu A \cdot L \cdot \mu mol^{-1}$. The limit of detection (LOD) was calculated from ($3 \times$ SDb/slope) [34], where SDb is the standard deviation of the blank measurements ($n = 10$). The obtained LOD value was 9.94 $\mu mol \cdot L^{-1}$.

Table 2 presents the concentration range, the experimental conditions, the applied technique and the LOD for other types of electrodes, which were recently reported for oxalic acid determination. As can be seen, the SBA/Nb/HpCo–CPE presents a LOD value comparable with the values of other electrodes. However, considering the concentration range above 1000 $\mu mol \cdot L^{-1}$, the SBA/Nb/HpCo–CPE electrode is among those with the lowest LOD values.

The SBA/Nb/HpCo–CPE was also used in the investigation of the electrochemical behavior of uric acid, using cyclic voltammetry and differential pulse voltammetry. Figure 8 shows the cyclic voltammograms for uric acid in the concentration range from 49 to 698 $\mu mol \cdot L^{-1}$, using 1 $mol \cdot L^{-1}$ KCl and a scan rate of 20 $mV \cdot s^{-1}$. In the absence of uric acid, no oxidation peak was detected. However, a well-defined and irreversible anodic peak was observed at a potential close to 0.35 V, thus characterizing the oxidation of uric acid by the SBA/Nb/HpCo–CPE.

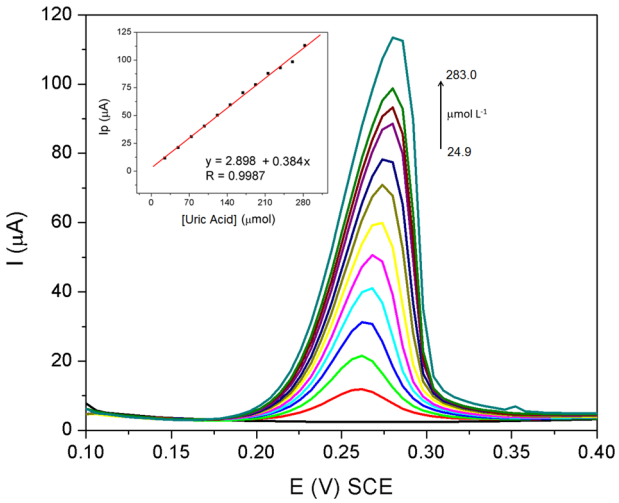

Fig. 10 Differential pulse voltammograms obtained with SBA/Nb/HpCo–CPE in the presence of different concentrations of uric acid, in phosphate buffer (0.1 $mol \cdot L^{-1}$, pH 6), KCl 1 $mol \cdot L^{-1}$ and $v = 5$ $mV \cdot s^{-1}$; The Inset shows the linear correlation between uric acid concentration and peak current intensity

With regard to the inset in Fig. 8, two linear concentration ranges are clearly identified.

The influence of the scan rate on the electrochemical behavior of uric acid was also investigated by cyclic voltammetry and the results are shown in Fig. 9. An increase in the current peak intensity and also a peak displacement to higher potentials were observed with increasing scan rate. Figure 9A provides information about the uric acid oxidation process, showing a linear correlation between the current peak intensity (Ip) and the square root of the scan rate ($v^{1/2}$). As observed for oxalic acid, this result also suggests that the mechanism of uric acid oxidation on the SBA/Nb/HpCo–CPE surface is controlled by diffusion of electroactive species [33]. However, the linear correlation between log Ip versus log v, which is presented in Fig. 9B,

Table 3 Comparative performance of different electrodes in the electrochemical determination of uric acid

Electrode	Experimental conditions	Electrochemical techniques	Linear range ($\mu mol \cdot L^{-1}$)	LOD ($\mu mol \cdot L^{-1}$)	Reference
GO/GCE[a]	PBS (0.1 M, pH 6.5) $v = 50\ mV \cdot s^{-1}$	CV	20–490	3.45	[43]
RGO-ZnO[b]	PBS (0.1 M, pH 6) $v = 50\ mV \cdot s^{-1}$ N_2 atmosphere	CV, DPV	1–70	0.33	[44]
Pd/RGO/GCE[c]	PBS (0.1 M, pH 7) $v = 0.05\ mV \cdot s^{-1}$	CV, DPV	6–470	1.6	[45]
GNP/FTO[d]	PBS (0.1 M, pH 7) $v = 100\ mV \cdot s^{-1}$	CV, DPV	10–100	0.28	[46]
Au-Cu_2O/rGO[e]	PBS (0.1 M), $v = 100\ mV \cdot s^{-1}$	CV, DPV, EIS	100–900	6.5	[47]
PB/rGO[f]	ABS (0.1 M, pH 6) $v = 25\ mV \cdot s^{-1}$	CV	40–415	8.0	[48]
NiO/MWCNT[g]	PBS (pH 7) $v = 50\ mV \cdot s^{-1}$	CV	10–2500	1	[49]
Fe_3O_4/CPE[h]	PBS (0.1 M, pH 7.5)	CV, EIS	160–2110	80	[50]
3D-ACNT[i]	PBS (0.01 M, pH 7.4) $v = 50\ mV \cdot s^{-1}$	CV	100–1000	1	[51]
SBA/Nb/HpCo–CPE	PBS (0.1 M, pH 6) KCl (0.1 M) $v = 20\ mV \cdot s^{-1}$	CV, DPV	25–350	0.17	This work
SBA/Nb/HpCo–CPE[j]	PBS (0.1 M, pH 6) KCl (0.1 M) $v = 20\ mV \cdot s^{-1}$	CV, DPV	98–260	0.14	This work

LOD Limit of detection, *EIS* Electrochemical impedance spectroscopy, *CV* Cyclic voltammetry, *DPV* Differential pulse voltammetry, *LSV* Linear sweep voltammetry, v = scan rate

[a]Uricase onto graphene oxide/glassy carbon electrode

[b]Graphene zinc oxide/glassy carbon electrode

[c]Palladium on reduced graphene oxide/glassy carbon electrode

[d]graphene nanoplatelet-modifiedfluorine-doped tin oxide electrode

[e]Au-Cu_2O nanoparticles/reduced graphene oxide

[f]Prussian blue/reduced graphene oxide

[g]Niquel oxide/multi-walled carbon nanotube

[h]Magnetite modified carbon paste electrode

[i]3D-aligned carbon nanotube

[j]Simultaneous analysis with Oxalic Acid

shows a slope of 0.765. This value of slope, between 0.5 and 1.0, indicates that the process is controlled simultaneously by diffusion and adsorption [32]. This adsorption can be explained by the high porosity of the electrodes containing nanostructured SBA and by the presence of the Nb_2O_5, which presents Lewis acid sites that can interact with the uric acid [12, 14].

Differential pulse voltammograms were obtained with SBA/Nb/HpCo–CPE for uric acid, by varying its concentration in the range from 24.9 to 283.0 $\mu mol \cdot L^{-1}$. The voltammograms are depicted in Fig. 10 and they show that the anodic peak current increases with increasing uric acid concentration. The inset to Fig. 10 shows a linear correlation between the anodic peak current and the uric acid concentration, within the applied concentration range. The sensitivity was determined from the slope of the calibration curve, whose value was 0.384 $\mu A \cdot L \cdot \mu mol^{-1}$. The calculated LOD was 0.17 $\mu mol \cdot L^{-1}$. Therefore, compared with the oxalic acid, the SBA/Nb/HpCo–CPE showed higher sensitivity toward uric acid.

Table 3 presents a comparison of the performance of different electrodes recently used for the determination of uric acid with that of SBA/Nb/HpCo–CPE. As can be seen in Table 3, the electrode developed in this work showed a lower LOD value when compared with other electrodes already reported. Therefore, the electrode proposed in this work showed high sensitivity in the determination of uric acid over a wide linear concentration range. These results are promising and indicate that this electrode can be used as a sensor to determine uric acid.

The reproducibility of the SBA/Nb/HpCo–CPE was evaluated using four similar electrodes. The cyclic voltammograms were made using 9.8 $mmol \cdot L^{-1}$ of oxalic acid and the

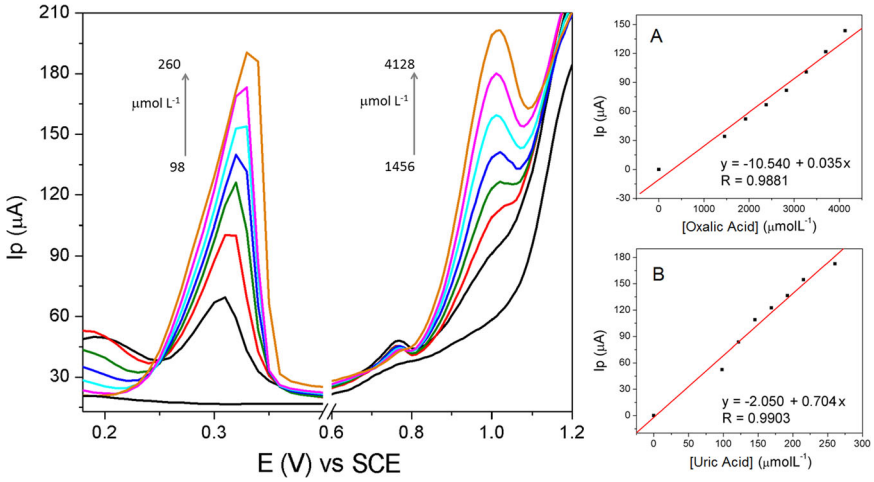

Fig. 11 Simultaneous analysis via differential pulse voltammetry for oxalic and uric acids using the SBA/Nb/HpCo–CPE, in phosphate buffer (0.1 mol·L^{-1}, pH 6) and KCl 1 mol·L^{-1} and $v = 20$ mV·s^{-1}; **A** linear correlation between oxalic acid concentration and peak current intensity; **B** linear correlation between uric acid concentration and peak current intensity

obtained standard deviation was 12.38%. In addition, the SBA/Nb/HpCo–CPE was evaluated using one electrode and 9.8 mmol·L^{-1} of oxalic acid. The standard deviation for six cycles, after 1 min of stirring and 2 min of rest, was 5.91%.

Taking into account the considerable oxidation peak separation between the two analytes, simultaneous analyses of oxalic and uric acids were also performed by differential pulse voltammetry, using SBA/Nb/HpCo–CPE, KCl 1 mol·L^{-1} and a scan rate of 20 mV·s^{-1}. The voltammograms, shown in Fig. 11, exhibit an increase in peak current after consecutive additions of oxalic acid and uric acid. Figure 11A shows the linear correlation between peak intensity versus oxalic acid concentration, within the range from 1456 to 4128 µmol·L^{-1}; whereas Fig. 11B presents the linear correlation for uric acid, in the concentration range between 98 and 260 µmol·L^{-1}. Based on these linear regressions, in the presence of both analytes, the sensitivities increased to 0.035 and 0.704 µA·L·µmol^{-1} for oxalic acid and uric acid, respectively. In this way, the calculated LOD values in the simultaneous evaluation of oxalic acid and uric acid have been decreased to 2.83 and 0.14 µmol·L^{-1}, respectively. These results indicate that the developed electrode (SBA/Nb/HpCo–CPE) allows the simultaneous evaluation of oxalic acid and uric acid concentrations with high sensitivity.

4 Conclusions

A high surface area mesoporous SBA-15 silica material with highly ordered and interconnected pore structure was obtained and successfully modified with niobium oxide (SBA/Nb). Afterwards, a further modification with CoHp was performed (SBA/Nb/HpCo). XRD and N_2 adsorption-desorption isotherms show that the modified material maintains the well-ordered pore structure as well as the textural properties of the SBA-15 silica material. The modified mesoporous material was used to manufacture a CPE (SBA/Nb/HpCo–CPE), which was applied to the evaluation of oxalic and uric acids by using cyclic voltammetry and differential pulse voltammetry, in a wide linear range of concentration. When compared with other reported electrodes, the modified CPE developed in this work presents the lowest LODs for uric acid. In addition, it allows the simultaneous evaluation of both analytes with high sensitivity, which makes it a very promising system for its applicability as a sensor for oxalic and uric acids.

Acknowledgements The authors thank CMM (Centro de Microscopia e Microanálise—UFRGS) and CNANO (Centro de Nanociência e Nanotecnologia—UFRGS) for the use of microscope and XRD equipment. The authors also thank the CBMM (Companhia Brasileira de Mineração e Metalurgia), which provided the $NbCl_5$ compound.

Funding The work was financially supported by CNPq (Conselho Nacional de Desenvolvimento Científico e Tecnológico, FAPERGS (Fundação de Amparo à Pesquisa do estado do Rio Grande do Sul) and CAPES (Coordenação de Aperfeiçoamento de Pessoal de Nível Superior).

Compliance with ethical standards

Conflict of interest The authors declare no competing interests.

Consent to participate All authors agree to participate in this work.

Consent for publication All authors agree on the content and its publication.

Publisher's note Springer Nature remains neutral with regard to jurisdictional claims in published maps and institutional affiliations.

References

1. Zhao D, Feng J, Huo Q, Melosh N, Fredrickson G, Chmelka B, Stucky G (1998) Triblock copolymer syntheses of mesoporous silica with periodic 50 to 300 angstrom pores. Science 279:548–552

2. Galarneau A, Cambon H, Renzo FD, Ryoo R, Choi M, Fajula F (2003) Microporosity and connections between pores in SBA-15 mesostructured silicas as a function of the temperature of synthesis. N J Chem 27:73–79
3. Gibson LT (2014) Mesosilica materials and organic pollutant adsorption: part A removal from air. Chem Soc Rev 43:5163–5172
4. Didó CA, Caneppele CDG, Schneid AC, Pereira MB, Costa TMH, Benvenutti EV (2018) Small gold nanoparticles with narrow size distribution achieved in SBA-15 pores by using ionic silsesquioxane instead of thiol group as stabilizer and adhesion agente. Micropor Mesopor Mater 270:48–56
5. Didó CA, Mass EB, Pereira MB, Hinrichs R, D'Oca MGM, Costa TMH, Russowsky D, Benvenutti EV (2020) Heterogeneous gold nanocatalyst applied in the synthesis of 2-aryl-2,3-dihydroquinazolin-4(1*H*)-ones. Colloids Surf A 589:124455
6. AbouAitah K, Lojkowski W (2021) Delivery of natural agents by means of mesoporous silica nanospheres as a promising anticancer strategy. Pharmaceutics 13:143
7. Tkachenko OS, Souza LV, Deon M, Becker EM, de Menezes EW, Arenas LT, Benvenutti EV (2021) AgNP-decorated SBA-15 for MWCNT paste modified electrode: a sensor for simultaneous voltammetric determination of paracetamol and sulfamethoxazole. Electroanalysis 33:29–37
8. de Souza LV, da Rosa DS, Tkachenko OS, Gomes AA, Costa TMH, Arenas LT, Benvenutti EV (2019) The role silica pore structure plays in the performance of modified carbon paste electrodes. Ionics 25:3259–3268
9. Pessoa CA, Gushikem Y, Kubota LT (2001) Ferrocenecarboxylic acid adsorbed on Nb_2O_5 film grafted on a SiO_2 surface: NADH oxidation study. Electrochim Acta 46:2499–2505
10. de Souza LV, Tkachenko O, Cardoso BN, Pizzolato TM, Dias SLP, Vasconcellos MAZ, Arenas LT, Costa TMH, Moro CC, Benvenutti EV (2019) Strategy to control the amount of titania dispersed on SBA-15 surface preserving its porosity, aiming to develop a sensor for electrochemical evaluation of antibiotics. Micropor Mesopor Mater 287:203–210
11. Kondo JN, Hiyoshi Y, Osuga R, Ishikawa A, Wang Y-H, Yokoi T (2018) Thin (single–triple) niobium oxide layers on mesoporous silica substrate. Micropor Mesopor Mater 262:191–198
12. Umpierres CS, Prola LDT, Adebayo MA, Lima EC, dos Reis GS, Kunzler DDF, Dotto GL, Arenas LT, Benvenutti EV (2017) Mesoporous Nb_2O_5/SiO_2 material obtained by sol–gel method and applied as adsorbent of crystal violet dye. Environm Technol 38:566–578
13. Sumiya S, Oumi Y, Sadakane M, Sano T (2009) Facile preparation of SBA-15-supported niobic acid ($Nb_2O_5{\cdot}nH_2O$) catalyst and its catalytic activity. Appl Catal A 365:261–267
14. Arenas LT, Villis PCM, Arguello J, Landers, Benvenutti EV, Gushikem Y (2010) Niobium oxide dispersed on a carbon ceramic matrix, $SiO_2/C/Nb_2O_5$, used as an electrochemical ascorbic acid sensor. Talanta 83:241–248
15. Xu X, Tian B, Zhang S, Kong J, Zhao D, Liu B (2004) Electrochemistry and biosensing reactivity of heme proteins adsorbed on the structure-tailored mesoporous Nb_2O_5 matrix. Anal Chim Acta 519:31–38
16. Chen Z, Prosperi M, Bird VY (2019) Prevalence of kidney stones in the USA: the National Health and Nutrition Evaluation Survey. J Clin. Urology 12:296–302
17. Zhang D, Li S, Zhang Z, Li N, Yuan X, Jia Z, Yang J (2021) Urinary stone composition analysis and clinical characterization of 1520 patients in central China. Sci Rep 11:6467
18. Dong X (2017) Study on detection methods for uric acid in biological samples. Int J Pharm Sci Res 8:926–929
19. Maiuolo J, Oppedisano F, Gratteri S, Muscoli C, Mollace V (2016) Regulation of uric acid metabolism and excretion. Int J Cardiol 213:8–14
20. Ensafi AA, Kazemzadeh A (2000) Flow injection spectrophotometric determination of ultra trace amounts of oxalic acid. Anal Chem 367:590–592
21. Khajehsharifi H, Pourbasheer E, Tavallali H, Sarvi S, Sadeghi M (2017) The comparison of partial least squares and principal component regression in simultaneous spectrophotometric determination of ascorbic acid, dopamine and uric acid in real samples. Arab J Chem 10:S3451–S3458
22. Wu FW, He ZK, Luo QY, Zeng YE (1999) HPLC determination of oxalic acid using tris(1,10-phenanthroline)ruthenium(II) chemiluminescence-application to the analysis of spinach. Food Chem 65:543–546
23. Li XL, Li G, Jiang YZ, Kang D, Jin CH, Shi Q, Jin T, Inoue K, Todoroki K, Toyo'oka T, Min JZ (2015) Human nails metabolite analysis: A rapid and simple method for quantification of uric acid in human fingernail by high-performance liquid chromatography with UV-detection. J Chromatogr B 1002:394–398
24. Zahavy E, Willner I (1996) Photoinduced electron transfer in eosin-modified Co(II)-protoporphyrin IX reconstituted myoglobin and α- or β-hemoglobin subunits: photocatalytic transformations by the reconstituted photoenzymes. J Am Chem Soc 118:12499–12514
25. Webb PA, Orr C, Camp RW, Olivier JP, Yunes YS (1997) Analytical methods in fine particle technology. Micromeritics Instrument Corporation, Norcross
26. Deon M, Caldas EM, Rosa DS, de Menezes EW, Dias SLP, Pereira MB, Costa TMH, Arenas LT, Benvenutti EV (2015) Mesoporous silica xerogel modified with bridged ionic silsesquioxane used to immobilize copper tetrasulfonated phthalocyanine applied to electrochemical determination of dopamine. J Solid State Electrochem 19:2095–2105
27. Pessoa CA, Gushikem Y (2001) Cobalt porphyrins immobilized on niobium (V) oxide grafted on a silica gel surface: study of the catalytic reduction of dissolved dioxygen. J Porphyr Phthalocya 5:537–544
28. Ribeiro ES, Dias SLP, Gushikem Y, Kubota LT (2004) Cobalt (II) porphyrin complex immobilized on the binary oxide SiO_2/Sb_2O_3: electrochemical properties and dissolved oxygen reduction study. Electrochim Acta 49:829–834
29. Pottier RH, Kennedy JC, Chow YFA (1988) The pKa values of hematoporphyrin-IX as determined by absorbance and fluorescence spectroscopy. Can J Spectr 33:57–62
30. Lucho AMS, Oliveira EC, Pastore HO, Gushikem Y (2004) 3-n-Propylpyridinium chloride silsesquioxane polymer film-coated aluminumphosphate and adsorption of cobalt(II)tetrasulphophthalocyanine: an electrocatalytic oxidation study of oxalic acid. J Electroanal Chem 573:55–60
31. Chollier MJ, Epron F, Lamy-Pitara E, Barbier J (1999) Catalytic oxidation of maleic and oxalic acids under potential control of platinum catalysts. Catal Today 48:291–300
32. Zhou Y, Tang W, Wang J, Zhang G, Chai S, Zhang L, Liu T (2014) Selective determination of dopamine and uric acid using electrochemical sensor based on poly(alizarin yellow R) film-modified electrode. Anal Methods 6:3474–3481
33. Brett AMO, Brett CMA (1996) Eletroquímica Princípios, Métodos e aplicações. Almeida, Coimbra
34. Currie LA (1995) Nomenclature in evaluation of analytical methods including detection and quantification capabilities (IUPAC Recommendations 1995). Pure Appl Chem 67:1699–1723
35. Fakhari AR, Rafiee B, Ahmar H, Bagheri A (2012) Electrocatalytic determination of oxalic acid by TiO_2 nanoparticles/multiwalled carbon nanotubes modified electrode. Anal Methods 4:3314–3319
36. Shang L, Zhao F, Zeng B (2013) Electrodeposition of PdAu alloy nanoparticles on ionic liquid functionalized graphene film for the voltammetric determination of oxalic acid. Electroanalysis 25:453–459

37. Raoof JB, Chekin F, Ehsani V (2015) Palladium-doped mesoporous silica SBA-15 modified in carbon-paste electrode as a sensitive voltammetric sensor for detection of oxalic acid. Sens Actuators B 207:291–296
38. Ma L, Zeng Q, Zhang M, Wang L, Cheng F (2016) Direct determination of oxalic acid by a bare platinum electrode contrasting a platinum nanoparticles-modified glassy carbon electrode. J Experim Nanosci 11:1242–1252
39. Rostami S, Azizi SN, Ghasemi S (2017) Preparation of an efficient electrocatalyst for oxalic acid oxidation based on Ag-doped ZSM-5 nanozeolites synthesized from bagasse. J Electroanal Chem 788:235–245
40. Kesavan L, Kalekar AM, Damlin P, Kvarnström C (2019) Reduced graphene oxide supported palladium nano-shapes for electro-oxidation of oxalic acid. J Electroanal Chem 847:113167
41. Nagarajan RD, Sundramoorthy AK (2019) One-pot electrosynthesis of silver nanorods/graphene nanocomposite using 4-sulphocalix[4]arene for selective detection of oxalic acid. Sens Actuators B 301:127132
42. Dodevska T, Shterev I (2020) Electrochemical non-enzymatic sensing of oxalic acid based on PdPt-modified electrodes: application to the analysis of vegetable samples. Monatsh Chem 151:495–504
43. Omar MN, Salleh AB, Lim HN, Tajudin AA (2016) Electrochemical detection of uric acid via uricase-immobilized graphene oxide. Anal Biochem 509:135–141
44. Zhang X, Zhang Y-C, Ma L-X (2016) One-pot facile fabrication of graphene-zinc oxide composite and its enhanced sensitivity for simultaneous electrochemical detection of ascorbic acid, dopamine and uric acid. Sens Actuators B 227:488–496
45. Wang J, Yang B, Zhong J, Yan B, Zhang K, Zhai C, Shiraishi Y, Du Y, Yang P (2017) Dopamine and uric acid electrochemical sensor based on a glassy carbon electrode modified with cubic Pd and reduced graphene oxide nanocomposite. J Colloid Interfac Sci 497:172–180
46. Rahman MM, Lopa NS, Ju MJ, Lee J-J (2017) Highly sensitive and simultaneous detection of dopamine and uric acid at graphene nanoplatelet-modified fluorine-doped tin oxide electrode in the presence of ascorbic acid. J Electroanal Chem 792:54–60
47. Aparna TK, Sivasubramanian R, Dar MA (2018) One-pot synthesis of Au-Cu_2O/rGO nanocomposite based electrochemical sensor for selective and simultaneous detection of dopamine and uric acid. J Alloy Compd 741:1130–1141
48. dos Santos PL, Katic V, Toledo KCF, Bonacin JA (2018) Photochemical one-pot synthesis of reduced graphene oxide/prussian blue nanocomposite for simultaneous electrochemical detection of ascorbic acid, dopamine, and uric acid. Sens Actuators B 255:2437–2447
49. Lal R, Bhatti MA, Shahzad G, Tahira A, Panhwar M, Lal B, Nafady A, Ibupoto ZH (2021) Chemically coupled multiwall carbon nanotubes with leaf-like nanostructures of NiO for sensitive and selective determination of uric acid. J Electron Mater 50:2852–2859
50. Erdogan ZO, Kucukkolbası S (2021) Fabrication of an electrochemical biosensor based on Fe_3O_4 nanoparticles and uricase modified carbon paste electrode for uric acid determination. Monatsh Chem 152:309–314
51. Yang M, Wang H, Liu P, Cheng J (2021) A 3D electrochemical biosensor based on Super-Aligned Carbon NanoTube array for point-of-care uric acid monitoring. Biosens Bioelectr 179:113082